Microfluid Nanofluid (2015) 19:1497–1505
DOI 10.1007/s10404-015-1663-4

RESEARCH PAPER

Sensitive optofluidic flow rate sensor based on laser heating and microring resonator

Yuan Gong[1,2,3] · Minglei Zhang[1] · Chaoyang Gong[1] · Yu Wu[1,3] · Yunjiang Rao[1] · Xudong Fan[2]

Received: 26 March 2015 / Accepted: 3 October 2015 / Published online: 17 October 2015

Abstract We demonstrate an optofluidic flow rate sensor based on the heat transfer effect in a microfluidic channel for the lab-on-a-chip applications. By employing an optofluidic ring resonator (OFRR), the wavelength shift of the resonant dip of the whispering gallery mode is detected as a function of the flow rate when the flow is heated by a 1480-nm laser. A measurement range of 2–100 μL/min, a minimum detectable change of 30 nL/min, and an accuracy of 5.2 % for the flow rate detection are achieved. Experimental results indicate that the OFRR flow rate sensor has good repeatability, and the inverse sensitivity is beneficial for detecting the low flow rate with high sensitivity.

Keywords Optofluidics · Flow rate sensor · Microring resonator · Heat transfer · Whispering gallery mode

Electronic supplementary material The online version of this article (doi:10.1007/s10404-015-1663-4) contains supplementary material, which is available to authorized users.

✉ Yuan Gong
ygong@uestc.edu.cn

[1] Key Laboratory of Optical Fiber Sensing and Communications (Ministry of Education), University of Electronic Science and Technology of China, Chengdu 611731, China

[2] Department of Biomedical Engineering, University of Michigan, Ann Arbor, MI 48109, USA

[3] Center for Information in BioMedicine, University of Electronic Science and Technology of China, Chengdu 611731, China

1 Introduction

Microfluidics has been a mainstream technology for a wide range of applications, such as the flow cytometry and the drug discovery (Whitesides 2006). In these applications, the flow rate plays an important role. In microfluidic cytometry and cell sorting, it is essential to measure the flow rate to determine the concentration of cells, by detecting the absolute cell counts in a specific volume (Hassan et al. 2014) or optimizing the efficiency of the counting or sorting process (Yang and Soh 2012). In the field of biopharmaceutical industry, the flow rate has a significant effect on the cell adhesion and proliferation as well as the monoclonal antibody production (Garza-García et al. 2014). The flow rate is also crucial for the microdroplet generation and influences both the size and the generation frequency (Stan et al. 2009; Riche et al. 2014; Keyon et al. 2014; Shih et al. 2015), and for the microfluidic production of liposomes (Zook and Vreeland 2010), hollow microspheres (Chen et al. 2012), and chitosan microfibers (He et al. 2015). A slight flow rate variation may lead to a size change of the products (Korczyk et al. 2011; Li et al. 2014). Thus, the precise control and measurement of the flow rate is highly desirable. In the literature, the flow rate is often controlled by a commercially available syringe pump. However, there is an evident delay from the pump to the microfluidic chip, especially with a long channel length and at a low flow rate. Therefore, the real-time, local detection of the flow rate in microfluidics is of great importance.

Current microfluidic flowmeters are based on the microelectromechanical systems (MEMS) (Nisar et al. 2008; Wu et al. 2001), the optical detection methods (König et al. 2010; Lien and Vollmer 2007; Cheri et al. 2014; Liu et al. 2014b), etc. The MEMS flowmeters have several distinct

advantages such as high integration and good sensing performance, but the fabrication process is complex (Wu et al. 2001), and in some cases it may only perform the contact measurements (Nezhad et al. 2013). The laser Doppler velocity sensor is commonly used (König et al. 2010). While it provides good sensing performance, it is difficult to integrate it with microfluidic chip. Optical detection methods generally have simple structures and high sensitivity.

Different kinds of physical effects have been employed for the flow rate sensing, including the trace particle or chemical detection (Santiago et al. 1998; Wu and Ye 2005), the flow force effect (Lien and Vollmer 2007; Cheri et al. 2014; Nezhad et al. 2013; Gervinskas et al. 2013), and the heat transfer effect (Liu et al. 2014b). The trace chemical detection method, including the microparticle image velocimetry (PIV; Santiago et al. 1998), is straightforward. The flow rate can be directly reflected by the spread of chemicals or micro-/nanoparticles and determined by chemical sensors or imaging. However, there may not be desired trace chemicals or micro-/nano-particles in the tested microfluid, and the injection of the additional trace chemicals or particles may influence the original biochemical functionality of the microfluidics. The flowmeter based on the flow force detection is also widely employed. Lien and Vollmer developed a microfluidic flow rate sensor with a wide dynamic range by a chemically etched fiber-tip cantilever. However, the sensitivity is low, and the microparticles or cells in the microfluid may be attached to the cantilever, causing additional errors in the flow rate measurement. The flowmeter based on the heat transfer effect has also been developed, as the heat transfer accelerates as the flow rate increases. One such example is by integrating a highly Co^{2+}-doped fiber with microfluidic capillaries to concomitantly heat and detect the temperature change of the microfluidic channels (Liu et al. 2014b). However, the multi-steps of stacking, tapering during the fabrication of the specialty fiber, and inscribing a microfiber Bragg grating (μFBG) in it makes the fabrication process time-consuming and costly. Therefore, developing a simple, integrated but contactless, highly sensitive flowmeter for microfluidics still remains a topic of research interest.

Optofluidic ring resonators (OFRRs) (Fan and White 2011; White et al. 2006; Zhu et al. 2007; Li and Fan 2010) have been developed as an excellent microfluidic platform by naturally integrating the microring resonator with a microfluidic channel. These high-Q microring resonator supports the whispering gallery modes (WGMs) and enables the highly sensitive, label-free detection of molecules (Zhu et al. 2007; Li and Fan 2010), tunable optofluidic device (Liu et al. 2014a), as well as novel optofluidic lasers (Fan and Yun 2014). During these optofluidic applications, the flow rate also plays important roles. Thus, we used the OFRR as an example for the demonstration of the flow rate detection. In this article, the microfluidic flow rate is determined by detecting the wavelength shift of the whispering gallery mode (WGM) of the OFRR caused by the heat transfer effect. The scheme can perform the local flow rate measurement along the capillary and has high sensitivity.

2 Principle

The WGM sensors have been widely used for the label-free biochemical detection (Foreman et al. 2015). In addition to various materials used, there are many different morphology styles of the WGM resonators, including the microspheres (Vollmer and Arnold 2008), microtoroid (Zhu et al. 2010), and hollow or solid microcylinders (Fan and White 2011; Rowland and Love 1993). Among them, the OFRR, by employing a hollow round capillary, perfectly integrates the functions of both the optical detection and the microfluidic flow. On the other hand, different coupling schemes have been demonstrated for the WGM sensors by using the free space optics, fiber tapers, and several kinds of microprisms (Zhu et al. 2014; Knight et al. 1997; White et al. 2005).

Here we use a fiber taper to couple the laser beam into the OFRR. Figure 1 shows the cross section of the structure. The fiber taper is perpendicular to the capillary, as shown in Fig. 2a. A small fraction of the incident light is coupled from the taper into the OFRR and is kept circulating in the wall of the OFRR due to the total internal reflection. The laser power stored in the OFRR increases rapidly and then reaches a stable status. After each round trip, a small fraction of light is coupled out to the fiber taper. The multiple output beams interfere with each other and the resonant dips are generated in the spectrum of the output beam. In case of the high Q factor WGM resonator, the full width at half magnitude (FWHM) of the linewidth is narrow and is helpful for the high-performance sensing.

The resonance wavelength of the OFRR is given by (Gorodetsky and Ilchenko 1999)

$$\lambda = \frac{2\pi r n_{\text{eff}}}{m}. \tag{1}$$

Here r is the radius of the OFRR, n_{eff} is the effective refractive index of the fundamental WGM and m is an integer. Compared with the higher-order radial modes, the fundamental mode is located near the outer surface of the capillary, corresponding to a larger radius and also a larger n_{eff} that is much less influenced by the index changes of the solution in the capillary. Considering the thermal expansion effect and thermo-optic effect, the wavelength shift can be expressed as (Fan et al. 2007; Suter et al. 2007).

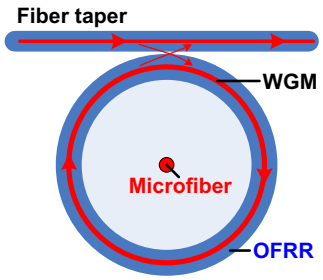

Fig. 1 Schematic cross section of the structure for the flow rate detection

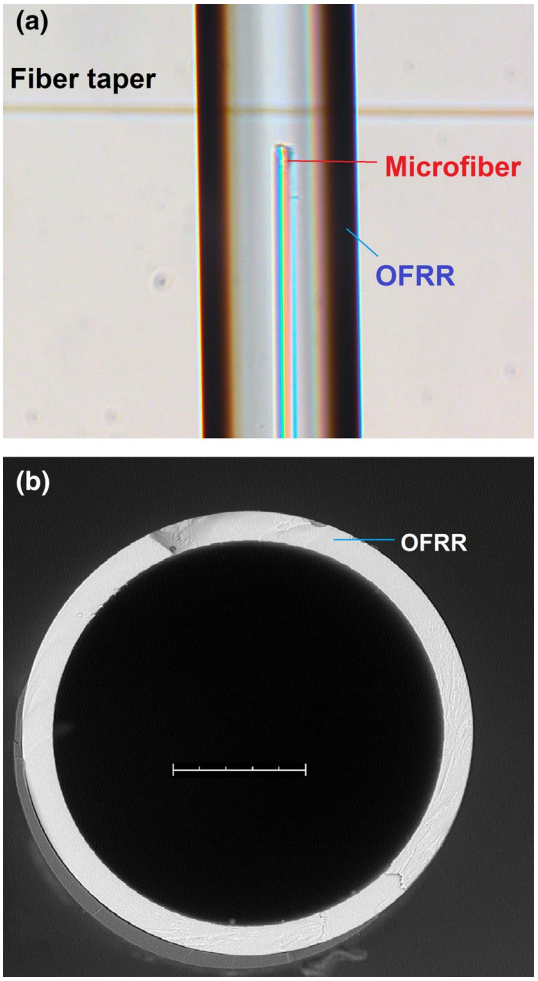

Fig. 2 **a** Microscopic image of the structure for the flow rate dection and **b** the SEM image of the cross section of the OFRR. *Bar* 50 μm

$$\frac{\Delta\lambda}{\lambda} = \left(\alpha + \frac{\kappa_{\text{wall}}}{n_{\text{eff}}}\frac{\partial n_{\text{eff}}}{\partial n_{\text{wall}}} + \frac{\kappa_{\text{core}}}{n_{\text{eff}}}\frac{\partial n_{\text{eff}}}{\partial n_{\text{core}}}\right)\Delta T. \quad (2)$$

Here $\alpha = 1/r(\partial r/\partial T)$ is the thermal expansion coefficient of the resonator and $\kappa_{\text{wall(core)}} = \partial n/\partial T$ is the thermo-optic effect for the wall (core). The "wall" is the solid part of the capillary, and the "core" means the hollow part within the capillary for the liquid to flow through. Note that it is different from the fiber core and cladding. Here the light propagates near the wall surface of the capillary, i.e., the OFRR. The microfiber in the center of the capillary, as shown in Fig. 1, with a laser beam emitted from its end face is only used for heating the solution.

Heat is firstly transferred from the microfiber tip to the inner liquid core and then to the silica ring resonator. From Eq. 2, one can see that there are three factors affecting the wavelength shift of the OFRR. The first is the thermal expansion of the silica microring, which is positive and also the dominant factor for the wavelength shift. The other two are the thermo-optical effects on the silica ring and liquid core, respectively. The thermo-optic coefficients for silica and water are $\kappa_{\text{wall}} = 5 \times 10^{-7}/°\text{C}$ and $\kappa_{\text{core}} = -8 \times 10^{-5}/°\text{C}$, respectively. Note that the latter is negative. Thus, the former two terms in Eq. 2 lead to a red shift of the resonant wavelength, whereas the third term leads to a blue shift. Since a relatively thick wall (~11 μm) is used in the OFRR in our experiment, the third term in Eq. 2 can be ignored, as $\partial n_{\text{eff}}/\partial n_{\text{core}}$ is negligible. Totally there is a red wavelength shift as the temperature increases, as indicated by the experimental results. $\partial n_{\text{eff}}/\partial n_{\text{core}}$ is negligible because we detect the fundamental radial mode, which is located near the outer surface of the capillary. The light intensity distribution, including the evanescent wave, of the fundamental radial mode will not penetrate into the inner liquid of the capillary. So the effective index of the fundamental radial mode will not be influenced by the refractive index changes of the liquid in the capillary.

In order to evaluate the influence of the displacement of the heating fiber tip from the center of the capillary on the sensing performance, we simulate the temperature distribution over the cross section of the OFRR. The heating fiber was intentionally adjusted away from the center of the cross section. Then the deformation, the optical path length (OPL) and finally the wavelength shift of the OFRR was numerically calculated. According to the simulations, the influence of a displacement of 10 μm of the heating fiber tip on the wavelength shift is negligible, see Fig. S1 in Supplementary Material.

3 Experimental setup

The flow rate sensing experiment is demonstrated in a silica capillary, i.e., the OFRR, which is employed simultaneously as the microfluidic channel and the non-contact optical detector. The OFRR is fabricated from a commercial capillary (Model CV1017Q, VitroCom), with an outer diameter of 170 μm and an initial inner diameter of 100 μm, respectively. The hydrofluoric (HF) acid is used to etch the inner wall and finally reduce the wall thickness

down to about 11 μm. Deionized water is firstly placed in an ultrasonic bath to reduce the air solubility in order to avoid potential bubble formation during the experiment and then used as a sample liquid for the flow rate sensing. The flow rate is controlled by a syringe pump (Model Pump 11 Elite, Harvard Apparatus).

A 1480-nm pump laser is used for heating the microfluid due to the high optical absorption coefficient of water in this spectral range. The laser is coupled into a fiber tip, which is inserted into the capillary to heat the microfluid (Fig. 2a). The fiber tip is fabricated by heating and drawing a single-mode fiber (SMF). The WGM shift of the OFRR is monitored by a wavelength-swept laser-based optical spectrum analyzer (OSA, Agilent), which is tunable between 1505 and 1620 nm. The resolution is set to be 0.2 pm. Light is coupled into and collected from the OFRR through a fiber taper with a waist of about 3 μm. The microscopic image, Fig. 2a, shows the relative position of the OFRR, the fiber taper for optical coupling, and the microfiber tip for heating. The SEM image of the cross section of the OFRR is shown in Fig. 2b.

4 Results and discussion

4.1 Demonstration and parametric investigation

Transmission spectra of the first OFRR (OFRR 1) at a flow rate of 10 μL/min under different heating laser powers are shown in Fig. 3a. The details of the monitored resonant dips are enlarged and shown in Fig. 3b. The HF acid with a concentration of 5 wt% was used for etching the wall of the OFRR down to about 11 μm. The microfiber tip with a diameter of 18 μm was used for the heating, and the core diameter is comparable to the laser wavelength, 1480 nm. The Q factor can be determined from the spectra to be around 2.3×10^4. The free spectral range (FSR) is about 3.0 nm, which is in good agreement with that calculated from $\mathrm{FSR} = \lambda^2/2\pi r n_{\mathrm{eff}}$.

Firstly, the flow rate, v, is kept constant at 10 μL/min. We monitor the wavelength shift, $\Delta\lambda$, as a function of the heating laser power, P_{heat}, as shown in Fig. 4 (black squares). After tuning the laser power, the heat transfer gets balanced in a few seconds. Then the resonant peak wavelength is recorded from the build-in fitting program of the OSA. A maximum wavelength shift of 839 pm is detected at a power of $P_{\mathrm{heat}} = 64.74$ mW under a flow rate of 10 μL/min. A linear relationship between the wavelength shift and the heating power is observed, which indicates that the laser-induced thermal effect leads to a linear change of the OPL of the monitored WGM. The slope for the flow rate of 10 μL/min is 12.56 pm/mW.

Then, we repeat the experiment by changing the flow rate from 10 to 100 μL/min with a step of 5 μL/min by

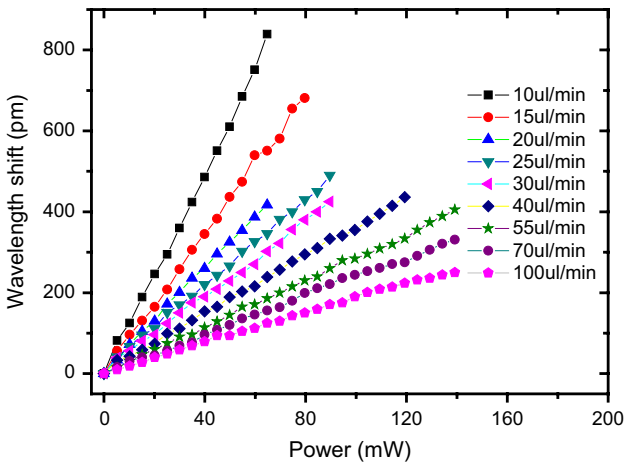

Fig. 4 Wavelength shift of the resonant dip for the OFRR 1 as a function of the heating power at different flow rates

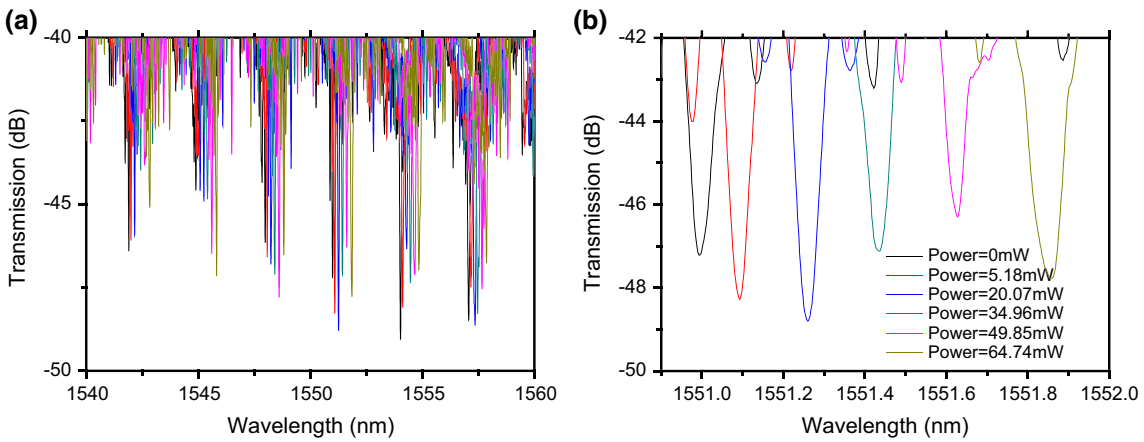

Fig. 3 Transmission spectra of the OFRR 1

setting the syringe pump. The wavelength shift is shown in Fig. 4 as a function of the heating power at different flow rates. The reference wavelength shift is set to be zero at the initial condition with no laser heating for each flow rate.

We re-plot in Fig. 5a with the same data from Fig. 4 to show the wavelength shift, $\Delta\lambda$, as a function of the flow rate, v, at different heating powers, P_{heat}. In the linear scale, the wavelength changes nonlinearly with the flow rate. The $\Delta\lambda - \Delta v$ sensitivity increases as the heating power increases and as the flow rate decreases. The maximum sensitivity in the linear scale is determined to be 57.6 pm per μL/min at a heating power of 64.74 mW with a flow rate of 10 μL/min. It is interesting that the wavelength changes linearly with the flow rate in the log–log scale, as shown in Fig. 5b. At higher flow rate and lower heating power, the sensitivity is low, and there are wavelength fluctuations as shown in Fig. 5b. The R square of the linear fitting for the data with the heating power of 64.74 mW is about 0.995 and the slope is about 0.81 ± 0.01.

The slope, $k = \partial\lambda/\partial P_{\text{heat}}$, of each $\Delta\lambda - P_{\text{heat}}$ curve in Fig. 4 is obtained by a linear fitting and shown as a function of the flow rate, v, in the linear scale (Fig. 6a) and in the log–log scale (Fig. 6b). The slope decreases nonlinearly from 12.56 pm/mW for 10 μL/min to 1.83 pm/mW for 100 μL/min, indicating a nonlinear sensitivity at different flow rate ranges. In the log–log scale, the slope changes linearly with the flow rate. The R square of the linear fitting is about 0.996 and the slope is about 0.82 ± 0.01.

Experimental results in Fig. 5 indicate that higher sensitivity can be obtained at the lower flow rate, v, with a higher heating power, P_{heat}. It is because more heat is transferred to the silica microring, thus leading to a larger temperature increment, ΔT, and a larger wavelength shift, $\Delta\lambda$ according to Eq. 2. In the current scheme, the maximum sensitivity of 57.6 pm per μL/min is mainly limited by the unwanted microbubble formation when the air solubility decreases as temperature increases (Xu et al. 2012). In this case, the heat transfer is disturbed by the bubble. At a flow

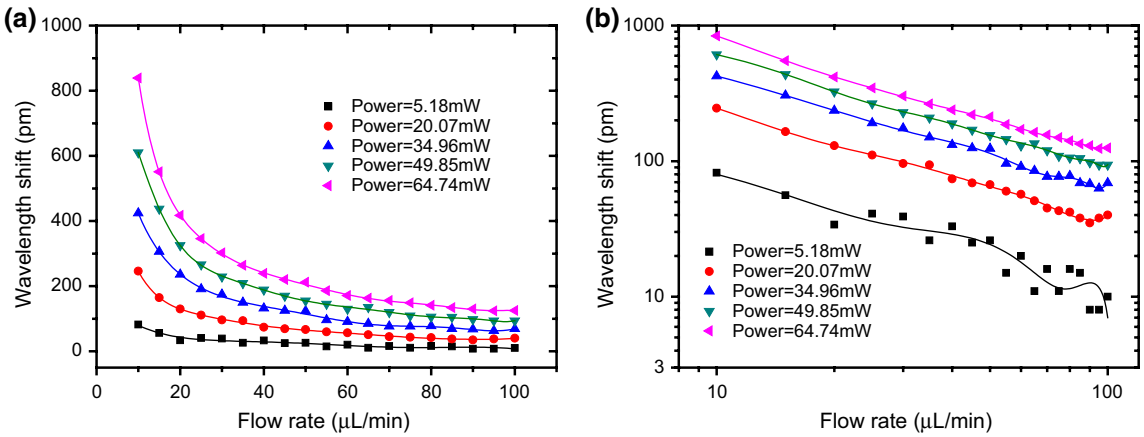

Fig. 5 Wavelength shift of the resonant dip for the OFRR 1 as a function of the flow rate at different heating powers in **a** the linear scale and **b** the log–log scale

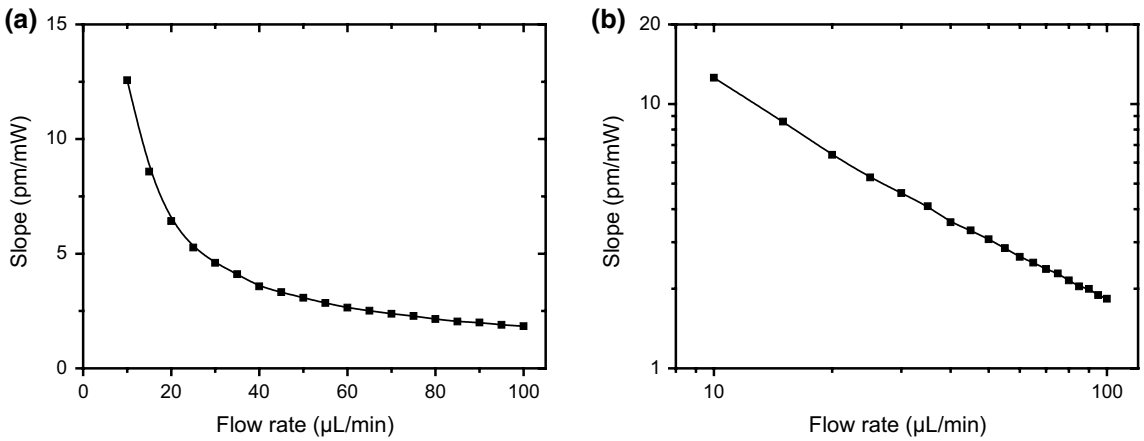

Fig. 6 Slope of the $\Delta\lambda - P_{heat}$ curve versus flow rate in **a** linear scale and **b** log–log scale

rate of 10 μL/min, microbubble formation at the fiber tip was occasionally observed in our experiment with heating power higher than 70 mW. There is a critical power density at each flow rate for bubble formation.

4.2 Flow rate sensing

Based on the results in the last section, we fixed the heating power at 53.7 mW for the flow rate detection to avoid the fluctuations at the low power range and also to avoid the bubble generation at the high power range. On the other hand, the structure was further optimized for the flow rate sensing. The microfiber tip for heating was fabricated with a cladding diameter of 13.3 μm and a core diameter of smaller than the heating laser wavelength. In this case the laser beam was not strongly confined within the fiber core anymore and spreads into a larger area compared to that of the heating microfiber in Sect. 4.1. It makes lower the laser density at the microfiber tip and further avoids the bubble generation at the low flow rate ranges. As a result, there is no bubble generation even with a static solution in the capillary, i.e., a flow rate of 0. It enables the lower flow rate detection in this section.

The inner wall of the silica capillary was etched by the HF acid with a concentration of 4 wt% for 520 min to obtain a wall thickness of about 11 μm. The etching rate is estimated to be 46 nm/min. The HF acid concentration is relatively lower than that used in Sect. 4.1 and better to obtain a OFRR with a higher Q factor. A diameter of 3.7 μm, instead of 3.1 μm in Sect. 4.1, for the fiber taper was also used to optimize the coupling of light into the OFRR.

The transmission spectra of the OFRR 2 with air and water in the capillary are shown in Fig. 7a, c, respectively. The details of typical resonant dips in each case were enlarged and shown in Fig. 7b, d. The FSRs of the fundamental WGM are 3.05 and 3.08 nm. The Q factors are 1.5×10^6 and 7.7×10^5. High Q factor is beneficial for the determination of the wavelength shift with a high resolution. The multiple resonant dips are clearly shown in Fig. 7d. The resonant dip with the largest fringe contrast is the one corresponding to the fundamental radial mode. Other dips correspond to higher-order WGMs and have gradually blueshifted resonant wavelengths, which are related with smaller n_{eff} and shorter OPL.

With a heating power of 53.7 mW, the calibration curve of the wavelength shift versus the flow rate was measured

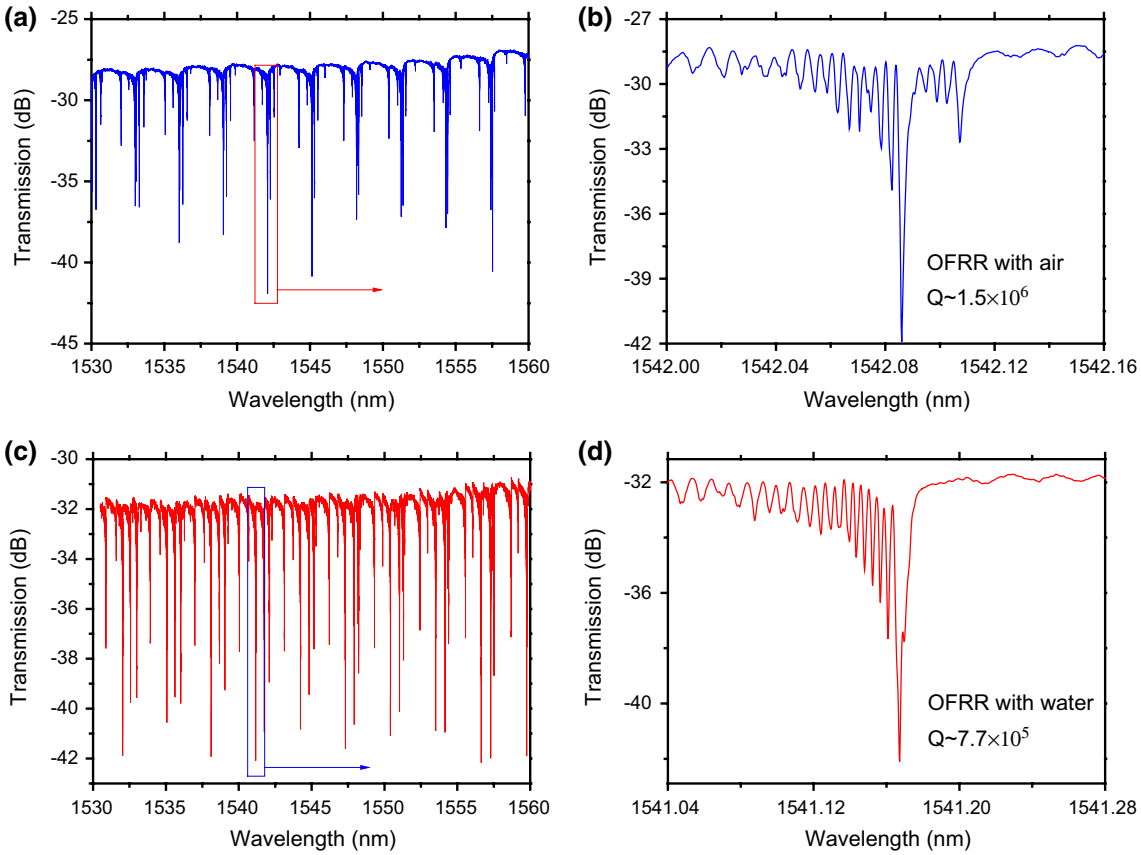

Fig. 7 Transmission spectra of the OFRR 2 with **a** air and **c** water in the capillary. **b** and **d** enlargely show typical resonant dips

and shown in the linear scale and the log–log scale in Fig. 8a, b, respectively. The error bar was calculated from the triplet measurements. The results indicate that the repeatability of the flow rate detection is good. The wavelength shift is set to be zero, $\Delta\lambda = 0$, at the initial condition with no laser heating for each flow rate, corresponds to the reference wavelength of λ_0. The data in Fig. 8a are fitted via $\Delta\lambda = av^b$ and the calibrated parameters are $a = 3386.6476$ and $b = -1.0442$. It is equivalent to the linear fitting of the data in Fig. 8b. The R square of the linear fitting is about 0.993. The fitting curves are also shown in Fig. 8a, b as the black lines.

The dynamic range of the flow rate detection is 2–100 μL/min. The flow rate in this range is particular important for the biochemical applications (Oates and Burgess 2012; Suter et al. 2008; Kim and Fan 2014; Rodriguez-Villarreal et al. 2010; Esquivel et al. 2012; Zhang et al. 2011).

To evaluate the minimum detectable flow rate change, δv, we tuned the flow rate from 2 μL/min with steps of 0.1, 0.4 and 0.6 μL/min and monitored the wavelength shift, as shown in Fig. 9. The step wavelength shifts are 35.2, 120.1, and 169.7 pm, respectively. During this measurement, the heating laser power was kept at 53.7 mW. The wavelength shift for a period of about 100 s at each flow rate was recorded. The averaged wavelength shifts during each period are also shown with blue lines in Fig. 9. The standard deviation (SD) of $\Delta\lambda_{min}$ is around ±3.4 pm for each flow rate, which originates partially from the flow rate variations from the syringe pump. The minimum detectable flow rate change, δv, is about 30 nL/min at a flow rate of 2 μL/min defined by the flow rate changes corresponds to that of three times of the SD of the wavelength shift, $3\Delta\lambda_{min} \sim \pm$ 10 pm. The minimum detectable flow rate change of the proposed method, δv, is about 30 times better than the integrated micro FBG flowmeter, 960 nL/min in the comparable flow rate range (Liu et al. 2014b).

In case of 5-mL syringe, the flow rate can be set by the syringe pump between 187 pL/min and 194 μL/min. The accuracy of ± 0.5 % was given by the manufacturer and at flow rate of 2 μL/min can be calculated to be ± 10 nL/min, comparable to δv. It is therefore the accuracy of the syringe pump that limits the minimum detectable flow rate change, δv, of the proposed sensor, which can be further improved by a better calibration setup. On the other hand, after the calibration, the sensor can be employed in case the microfluidic pumping methods other than the syringe pump are used. Except for the syringe pump, there were various pumping schemes recently developed, including on-chip peristaltic pump (Bowen and Martin 2010), electrochemical pump (Xie et al. 2004), piezoelectric pump (Palmieri 2015), or even pumpless flow control (Marimuthu and Kim 2013). These pump schemes may have lower accuracy of

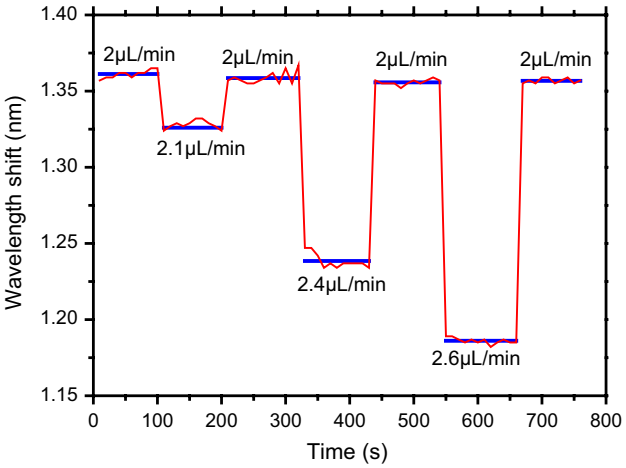

Fig. 9 Wavelength shift versus time with step changes of the flow rate near 2 μL/min

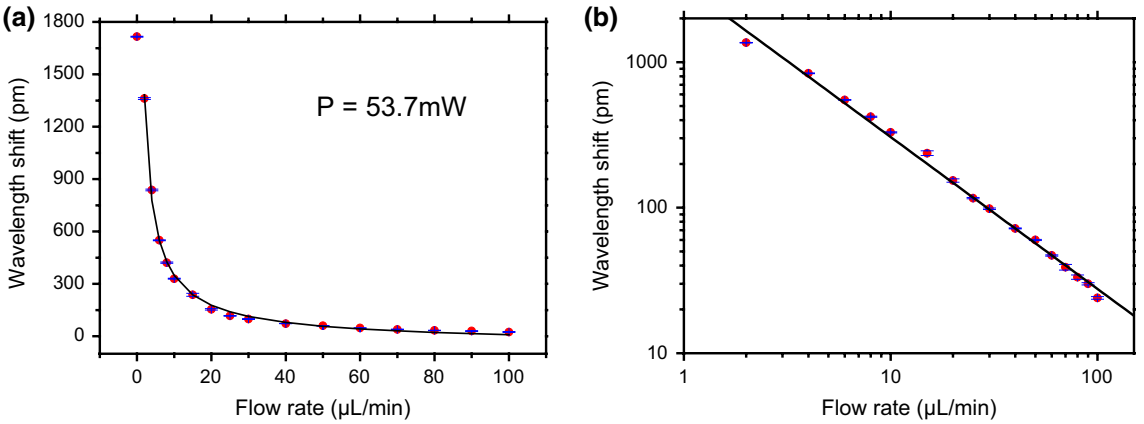

Fig. 8 Calibration curve of the wavelength shift versus the flow rate in **a** linear scale and **b** log–log scale. *Error bars* are based on triplet measurements

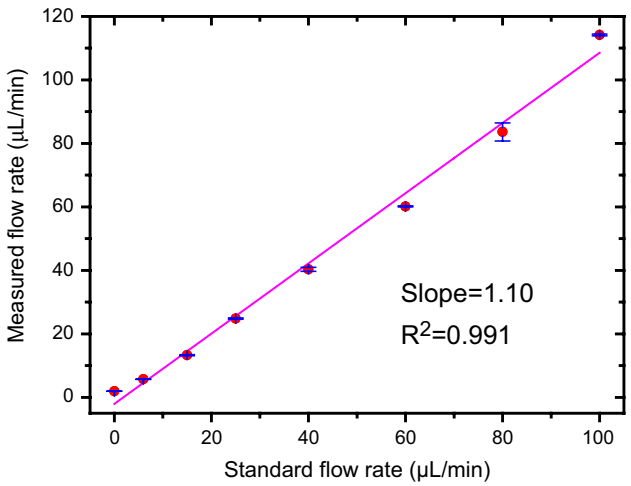

Fig. 10 Flow rate measured by the OFRR versus standard flow rate controlled by the syringe pump. *Error bars* are based on triplet measurements

flow control, and a high sensitivity flow rate sensor is helpful for providing a feedback signal and further enhancing the flow controlling performance.

After the calibration, we measured the standard flow rate by the detected wavelength, λ, and the calibrated parameters via $v = \left((\lambda - \lambda_0)/a\right)^{1/b}$. The measured flow rate is plotted as a function of the standard flow rate controlled by the syringe pump, as shown in Fig. 10. The R square of the linear fitting is about 0.991, and the slope is about 1.10 ± 0.02. The accuracy was calculated from the deviation between the measured flow rate and the standard flow rate, that is, $A = \text{abs}(v_m - v_s)/v_s$, abs denotes for the absolute value of the deviation, v_m is the flow rate measured based on the wavelength shift and the calibration formula, v_s is the standard flow rate generated by the syringe pump. The accuracy is determined statistically to be about 5.2 %, which is comparable to the accuracy of 5 % the commercial flow meters in the similar dynamic range, see the Table S1 in Supplementary Material.

5 Conclusion

An optofluidic flow rate sensor has been demonstrated by detecting the resonant wavelength shift of the WGM of an optofluidic ring resonator while heating the flow with another optical microfiber tip. The proposed flowmeter has the advantages of high flexibility and can perform local flow rate detection, especially for capillary-based microfluidics while not degrading other functionalities of the microring resonator including the biochemical sensing or optofluidic lasing.

Acknowledgments This work is supported by National Natural Science Foundation of China (61575039, 61475032, and 61290312), Program for Changjiang Scholars and Innovative Research Team in University (PCSIRT, IRT1218), and the 111 Project (B14039).

References

Bowen AL, Martin RS (2010) Integration of on-chip peristaltic pumps and injection valves with microchip electrophoresis and electrochemical detection. Electrophoresis 31:2534–2540

Chen R, Dong PF, Xu JH, Wang YD, Luo GS (2012) Controllable microfluidic production of gas-in-oil-in-water emulsions for hollow microspheres with thin polymer shells. Lab Chip 12:3858–3860

Cheri MS, Latifi H, Sadeghi J, Moghaddam MS, Shahraki H, Hajghassem H (2014) Real-time measurement of flow rate in microfluidic devices using a cantilever-based optofluidic sensor. Analyst 139:431–438

Esquivel JP, Castellarnau M, Senn T, Löchel B, Samitier J, Sabaté N (2012) Fuel cell-powered microfluidic platform for lab-on-a-chip applications. Lab Chip 12:74–79

Fan X, White IM (2011) Optofluidic microsystems for chemical and biological analysis. Nat Photon 5:591–597

Fan X, Yun SH (2014) The potential of optofluidic biolasers. Nat Methods 11:141–147

Fan X, White IM, Zhu H, Suter JD, Oveys H (2007) Overview of novel integrated optical ring resonator bio/chemical sensors. Proc SPIE 6452:64520M

Foreman MR, Swaim JD, Vollmer F (2015) Whispering gallery mode sensors. Adv Opt Photon 7:168–240

Garza-Garcia LD, Garcia-Lopez E, Camacho-Leon S, del Refugio Rocha-Pizaña M, López-Pacheco F, López-Meza J, Araiz-Hernandez D, Tapia-Mejia EJ, Trujillo-de Santiago G, Rodriguez-Gonzalez CA, Alvarez MM (2014) Continuous flow micro-bioreactors for the production of biopharmaceuticals: the effect of geometry, surface texture, and flow rate. Lab Chip 14:1320–1329

Gervinskas AS, Ghanbari M, Agudelo CG, Packirisamy M, Bhat RB, Geitmann A (2013) PDMS microcantilever-based flow sensor integration for lab-on-a-chip. IEEE Sens J 13:601–609

Gorodetsky ML, Ilchenko VS (1999) Optical microsphere resonators: optimal coupling to high-Q-whispering-gallery modes. J Opt Soc Am B 16:147–154

Hassan U, Watkins NN, Edwards C, Bashir R (2014) Flow metering characterization within an electrical cell counting microfluidic device. Lab Chip 14:1469–1476

He XH, Wang W, Deng K, Xie R, Ju XJ, Liu Z, Chu LY (2015) Microfluidic fabrication of chitosan microfibers with controllable internals from tubular to peapod-like structures. RSC Adv 5:928–936

Keyon ASA, Guijt RM, Bolch CJ, Breadmore MC (2014) Droplet microfluidics for postcolumn reactions in capillary electrophoresis. Anal Chem 86:11811–11818

Kim KH, Fan X (2014) Surface sensitive microfluidic optomechanical ring resonator sensors. Appl Phys Lett 105:191101

Knight JC, Cheung G, Jacques F, Birks TA (1997) Phase-matched excitation of whispering-gallery-mode resonances by a fiber taper. Opt Lett 22:1129–1131

König J, Voigt A, Büttner L, Czarske J (2010) Precise micro flow rate measurements by a laser Doppler velocity profile sensor with time division multiplexing. Meas Sci Technol 21:074005

Korczyk PM, Cybulski O, Makulska S, Garstecki P (2011) Effects of unsteadiness of the rates of flow on the dynamics of formation of droplets in microfluidic systems. Lab Chip 11:173–175

Li H, Fan X (2010) Characterization of sensing capability of optofluidic ring resonator biosensors. Appl Phys Lett 97:011105

Li Z, Mak SY, Sauret A, Shum HC (2014) Syringe-pump-induced fluctuation in all-aqueous microfluidic system implications for flow rate accuracy. Lab Chip 14:744–749

Lien V, Vollmer F (2007) Microfluidic flow rate detection based on integrated optical fiber cantilever. Lab Chip 7:1352–1356

Liu Y, Shi L, Xu XB, Zhao P, Wang ZQ, Pu SL, Zhang XL (2014a) All-optical tuning of a magnetic-fluid-filled optofluidic ring resonator. Lab Chip 14:3004–3010

Liu Z, Tse MV, Zhang AP, Tam HY (2014b) Integrated microfluidic flowmeter based on a micro-FBG inscribed in Co^{2+}-doped optical fiber. Opt Lett 39:5877–5880

Marimuthu M, Kim S (2013) Pumpless steady-flow microfluidic chip for cell culture. Anal Biochem 437:161–163

Nezhad AS, Ghanbari M, Agudelo CG, Packirisamy M, Bhat RB, Geitmann A (2013) PDMS microcantilever-based flow sensor integration for lab-on-a-chip. IEEE Sens J 13:601–609

Nisar A, Afzulpurkar N, Mahaisavariya B, Tuantranont A (2008) MEMS-based micropumps in drug delivery and biomedical applications. Sens Actuators B 130:917–942

Oates TC, Burgess LW (2012) Sensitive refractive index detection using a broad-band optical ring resonator. Anal Chem 84:7713–7720

Palmieri M (2015) Piezoelectric microfluidic pumping device and method for using the same. US Patent No. 08956325

Riche CT, Zhang C, Gupta M, Malmstadt N (2014) Fluoropolymer surface coatings to control droplets in microfluidic devices. Lab Chip 14:1834–1841

Rodriguez-Villarreal AI, Arundell M, Carmona M, Samitier J (2010) High flow rate microfluidic device for blood plasma separation using a range of temperatures. Lab Chip 10:211–219

Rowland DR, Love JD (1993) Evanescent wave coupling of whispering gallery modes of a dielectric cylinder. IEE Proc J 140:177–188

Santiago JG, Wereley ST, Meinhart CD, Beebe DJ, Adrian RJ (1998) A particle image velocimetry system for microfluidics. Exp Fluids 25:316–319

Shih SCC, Gach PC, Sustarich J, Simmons BA, Adams PD, Singh S, Singh AK (2015) A droplet-to-digital (D2D) microfluidic device for single cell assays. Lab Chip 15:225–236

Stan CA, Tang SK, Whitesides GM (2009) Independent control of drop size and velocity in microfluidic flow-focusing generators using variable temperature and flow rate. Anal Chem 81:2399–2402

Suter JD, White IM, Zhu H, Fan X (2007) Thermal characterization of liquid core optical ring resonator sensors. Appl Opt 46:389–396

Suter JD, White IM, Zhu H, Shi H, Caldwell CW, Fan X (2008) Label-free quantitative DNA detection using the liquid core optical ring resonator. Biosens Bioelectron 23:1003–1009

Vollmer F, Arnold S (2008) Whispering-gallery-mode biosensing: label-free detection down to single molecules. Nat Methods 5:591–596

White IM, Hanumegowda NM, Fan X (2005) Subfemtomole detection of small molecules with microsphere sensors. Opt Lett 30:3189–3191

White IM, Oveys H, Fan X (2006) Liquid-core optical ring-resonator sensors. Opt Lett 31:1319–1321

Whitesides GM (2006) The origins and the future of microfluidics. Nature 442:368–373

Wu J, Ye J (2005) Micro flow sensor based on two closely spaced amperometric sensors. Lab Chip 5:1344–1347

Wu S, Lin Q, Yuen Y, Tai YC (2001) MEMS flow sensors for nanofuidic applications. Sens Actuators A 89:152–158

Xie J, Miao YN, Shih J, He Q, Liu J, Tai YC, Lee TD (2004) An electrochemical pumping system for on-chip gradient generation. Anal Chem 76:3756–3763

Xu R, Xin H, Li Q, Yang X, Chen H, Li B (2012) Photothermal formation and targeted positioning of bubbles by a fiber taper. Appl Phys Lett 101:054103

Yang AHJ, Soh HT (2012) Acoustophoretic Sorting of Viable Mammalian Cells in a Microfluidic Device. Anal Chem 84:10756–10762

Zhang K, Jian A, Zhang X, Wang Y, Li Z, Tam H (2011) Laser-induced thermal bubbles for microfluidic applications. Lab Chip 11:1389–1395

Zhu HY, White IM, Suter JD, Dale PS, Fan X (2007) Analysis of biomolecule detection with optofluidic ring resonator sensors. Opt Express 15:9139–9146

Zhu J, Ozdemir SK, Xiao YF, Li L, He L, Chen DR, Yang L (2010) On-chip single nanoparticle detection and sizing by mode splitting in an ultrahigh-Q microresonator. Nat Photon 4:46–49

Zhu J, Ozdemir SK, Yilmaz H, Peng B, Dong M, Tomes M, Carmon T, Yang L (2014) Interfacing whispering-gallery microresonators and free space light with cavity enhanced Rayleigh scattering. Sci Rep 4:6396

Zook JM, Vreeland WN (2010) Effects of temperature, acyl chain length, and flow-rate ratio on liposome formation and size in amicrofluidic hydrodynamic focusing device. Soft Matter 6:1352–1360